Supplementary Information

Zahra Zarei,[a] John Berezney,[a] Alexander Hensley,[a] Linnea Lemma,[b]

Nesrin Senbil,[a] Zvonimir Dogic,[c] and Seth Fraden[a]

[a] *The Martin Fisher School of Physics, Brandeis University, Waltham, Massachusetts 02454, USA.*
Email: fraden@brandeis.edu
[b] *The Department of Chemical and Biological Engineering, Princeton, NJ 08544, USA.*
[c] *Department of Physics, University of California, Santa Barbara, California 93106, USA.*

Table of Contents

1 DLP Calibration

Flattening the light intensity

The patterned illumination was generated using a Digital Light Processor (DLP) (EKB4500MKII P2, EKB Technologies Ltd) whose lens projects light onto a 20.4 mm by 12.7 mm image with a 25 mm working distance. The size of the projected image can be increased by removing a limit screw from the zoom lens and decreasing the working distance by a few millimeters. The projector incorporates a Digital Micromirror Device (DMD) made up of tiny mirrors that can be individually manipulated to generate a desired light pattern. The light pattern is transmitted to the DLP through MATLAB software. After projecting a flat field onto the sample plane, vignetting, a reduction of the image's brightness toward the periphery compared to the image center, occurs.

To quantify vignetting, the intensity of the projected pattern was quantified by placing a sensor (AVT Guppy F-146B) in the sample plane. The small camera was easily fitted on the sample plane of the Nikon Eclipse microscope, and was easily modified to access the bare sensor. The bare sensor was attached to a custom-made holder and mounted to the nosepiece on the Nikon microscope.(Supplementary Figure 1). The camera sensor was too small to capture the entire projected field. Therefore, the sensor was programmatically moved to different locations and multiple images were taken with 20 percent overlap and stitched together to create a composite image. This allowed for a quantitative analysis of the projected light intensity across the sample, which is essential for correcting vignetting effects. To improve accuracy, the 1 mm by 1 mm central part of the sensor was used.

To correct for vignetting we created a mapping between the projected light pattern and measured pixel values at each location. This mapping takes into account the nonlinear relationship between the projected

and measured intensity values as a function of $x - y$ position of the pixel on the DLP plane. Using the lookup table, the intensity values in the DLP plane can be selected to achieve the desired intensity for a given location in the sample plane (Supplementary Figure 3, 4).

The gaps between the mirrors in the DMD cause the measured intensity to fluctuate at a high spatial frequency. The DLP lens was defocused to smooth out the intensity fluctuations, but the resulting blurriness limited the sharpness of projected patterns (Supplementary Figure 2).

Spatial Calibration

An essential aspect of using the DLP is the spatial alignment of the field of view with the projected pattern. Multiple channels may require different intensities of light making it essential to relate the physical location of samples to the regions of the DLP that illuminate them. To ensure accurate alignment between the microscope field of view and the projected image, we determined the transformation matrix that maps the coordinates of the projected pattern to the coordinates of the measured image. This was done using a test pattern, which is first projected onto the sample plane and then imaged with the microscope camera. The coordinates of the corners of the test pattern in the projected image and the corresponding coordinates in the measured image were used to determine the affine transformation matrix between the two coordinate systems. Once determined, transformation matrix can be applied to the coordinates of each channel in the projected image to map them to the corresponding coordinates in the measured image. This defined the borders of each channel, enabling the light to be projected to the appropriate channels while ensuring that the correct intensities were applied.

It is important to determine the transformation matrix to accurately align the field of view and projection. This may require some experimentation and fine-tuning to achieve the desired results. It is also essential to use a sufficiently complex test pattern that contains a sufficient number of corners or other distinctive features to determine the transformation matrix accurately. The employed transformation matrices were:

$$\begin{bmatrix} \cos\theta & -\sin\theta & 0 \\ \sin\theta & \cos\theta & 0 \\ 0 & 0 & 1 \end{bmatrix} : \text{Rotation} \quad \begin{bmatrix} s & 0 & 0 \\ 0 & s & 0 \\ 0 & 0 & 1 \end{bmatrix} : \text{Scaling} \quad \begin{bmatrix} 1 & 0 & t_x \\ 0 & 1 & t_y \\ 0 & 0 & 1 \end{bmatrix} : \text{translation} \tag{1}$$

2 Experimental setup

The data were acquired with two different experimental setups. In the first system, the experimental chamber was fabricated by sandwiching two pieces of parafilm between a microscope slide (Supplementary Figure. 5a). The flow cell had dimensions of 3 mm length and 3 mm width, with a height of approximately 100 um. The epi-illumination branch of a Nikon microscope was used for both the computer controlled DLP that provided the blue light source for opto-activation of the motors and the fluorescence illumination used for imaging. This setup was primarily used to analyze the velocity field.

In the second configuration, the glass treatment was same but up to six channels containing active nematics were employed. These channels varied in width from 3 mm to 6 mm , with a length of 18 mm. The computer-controlled projector provided spatio-temporal patterns of blue light used to activate the opto-kinesin clusters. The DLP projector was mounted onto the sample stage and projected light from above onto the sample and into the objective located below the sample in a transmission illumination geometry.When the stage moved, the pattern of projected light with respect to the sample did not change. A separate optical arm in the reflection illumination geometry was used to illuminate and record the nematic director using fluorescence microscopy. High resolution images of the entire sample were obtained by scanning the stage across the microscope objective. The second geometry was primarily used to analyze the defects in the nematic field (Supplementary Figure. 5b).

3 Characterization of opto-K401

Supplementary Figure 6 represents the active nematic powered by K401-iLID micro pairs in the dark and illuminated area. We constructed a 2D active nematic from K401-iLid micro pairs and illuminated half left, while half right was not illuminated. To quantify the speed, we calculated the nematic speed in both regions using PIVlab [1, 2], and we determined the nematic flow speed in the dark region was

approximately 500 nm/sec. (Supplementary Video 1 for the illuminated and Supplementary Video 2 for the dark side) and the ratio of speeds between the light and dark regions was only a factor of six.

4 Transient nematic speed after a change in intensity

In Supplementary Figure 7, we measure the nematic speed as a function of intensity. We followed the same two-step preparation strategy explained in the paper. Before measuring the speed at a given intensity, we performed a two-step preparation protocol: "anneal" and "rest." The anneal process involved lighting the sample at a high, sustaining intensity of 20 mW/cm^2 for 4 minutes, followed by a 3 minute rest period. This data shows the experiment's reproducibility shown in Fig 3 (a,b,c,d), and the corresponding nematic speed vs. intensity is shown in Supplementary Figure 8 which confirms the reproducibility of Fig 3 (e).

Here, regions 1 and 3 were illuminated with 0.13 mW/cm^2, and region 2 was illuminated with 2.1 mW/cm^2. The defects vary in size near the walls, and the fluorescent image is low quality, so the MATLAB code [3] fails to find defects accurately. To solve this problem, the plotted defects are identified manually in supplementary Figure 10 a,b,c panel (i, ii). The nematic speed in each region is calculated using PIV, and the average nematic speed is averaged 1.5 mm away from the walls, illustrated in Supplementary Figure 10d. To find the average defect density for each region, the defect density was identified using the MATLAB script[3] and averaged 1.5 mm away from the walls, shown in Supplementary Figure 10e. As mentioned in the main manuscript, we changed the applied light intensity pattern after 33 minutes, therefore the regions 1 and 3 were illuminated with 2.1 mW/cm^2 and regions 2 was illuminated with 0.13 mW/cm^2.

To determine the time constants which describe the transient flow response, we introduce the normalized speed $|v_n(t)|$ as the instantaneous speed $|v(t)|$ divided by the steady-state speed $|v_s(t)|$. Supplementary Figure. 9(a) plots the normalized speed ($|v(t)|/|v_s(t)|$) against the time (t) following an increase in intensity from 0 to I. This data shows that after the applied light is increased, the resultant flow speed increases until saturation. The time over which the sample takes to reach this saturated flow speed decreases as the applied light intensity is increased. We fit this data to an exponential $|v_n(t)|^{\text{start}} = 1 - \exp(-t/\tau_{\text{start}})$ and plot the time constant for the nematic to reach its steady-state speed after starting from rest (τ_{start}) as a function of the light intensity.

In Supplementary Figure. 9(b), we plot the normalized speed against the time after the light is extinguished. To quantify this speed, the normalized speed is fit to an exponential of the form $|v_n(t)|^{\text{stop}} = (1 + \exp((t - t_0)/\tau_{\text{stop}}))^{-1}$, in which τ_{stop} is the time constant for the speed to decrease to zero and t_0 is the time delay between extinguishing the illumination and for the speed to begin to decrease. This data illustrates the reproducibility of the experiment shown in Fig 4.

5 Effect of the chamber walls on nematic speed and defect density

To study the effect of the chamber walls on the nematic speed and defect density, we constructed a large channel, 18 mm length and 5.3 mm width, using the experimental geometry shown Supplementary Figure 5(b). A zone of 12.8 mm in length by 5.3 mm in width was illuminated with blue light of 460 nm. This zone was divided into 3 contiguous areas of equal size, 5.3 mm in width and 4.3 mm in length, each with a different intensity (Supplementary Figure 10). The defect density and the nematic speed were measured across the three different zones.

6 Gradients in defect density and nematic speed as a function of distance from a boundary

The averaged defect density and nematic speed at the center of the channel for the experiment explained in Supplementary Figure 10 over both light patterns are presented in Table S1.

The reason for the spatial gradient in the defect density in Supplementary Figure 10 panel (i) is unclear. One possibility is that the oil gradient near the boundaries may cause the gradient. We made a 3 mm width and 3 mm length chamber using experimental geometry Supplementary Figure 5a. We captured multiple images using confocal microscopy at different depths in the sample close to the wall to quantify the oil

gradient. The nematic layer showed the location of the oil surface, and by analyzing the series of images, we could identify where the oil layer was positioned. To account for the oil's index of refraction, which is 1.29, the measured height was divided by this value. The point where the nematic layer is uniform was used as the reference point for the oil height axis. The result is illustrated in Supplementary Figure 11. There is a separation in length scales between the change in oil height from the boundary and the change in defect density. The oil height reaches a plateau value at 50 μm from the wall while the defect density plateaus at 1000 μm from the wall. Because of this separation in length scales we do not believe that the oil height causes the gradient in the defect density.

7 Additional Supplementary Figures and Tables
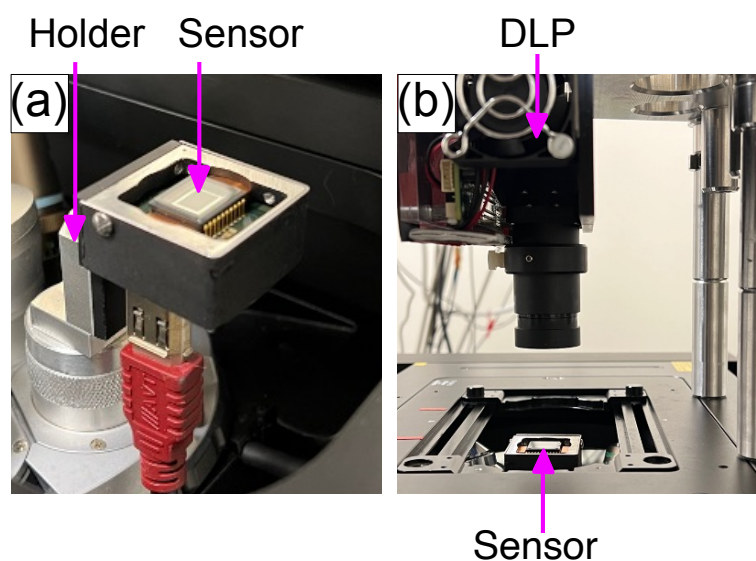
Supplementary Figure. 1 – **Correcting vignetting of the DLP.** (a)The CCD camera is utilized for calibration of projected light intensity. To access the sensor, the body of the camera is opened and as much of the housing is removed as possible. The sensor is mounted onto the Nikon nosepiece using custom machined holder. The overall size of the sensor array is 4.65 mm by 4.65 mm.(b) The DLP is attached to the sample stage which ensured that the projected light pattern moves with the stage. The sensor measures the light intensity projected by the DLP in the sample plane. The illumination wavelength is 460nm (center point).
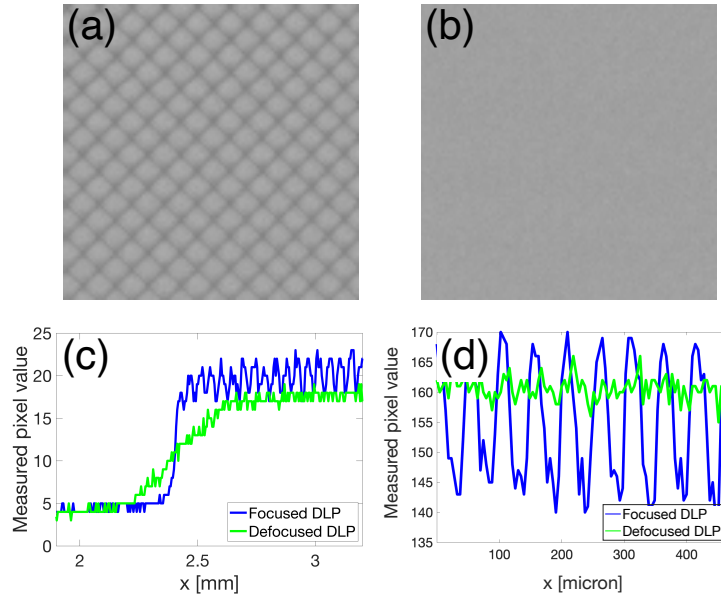
Supplementary Figure. 2 – **The effect of defocusing the DLP lens.** (a) Focused lens, so each mirror is visible on the sample plane. (b) Defocused lens. (c) The light intensity profile at the interface between low and high light intensities for a focused DLP (in blue) and a defocused DLP (in green). The focused DLP profile exhibits a sharp transition in intensity, while the defocused DLP profile shows a linear variation of intensity over a distance of 0.5 mm.(d) The intensity as a function of distance for the focused and defocused lens.
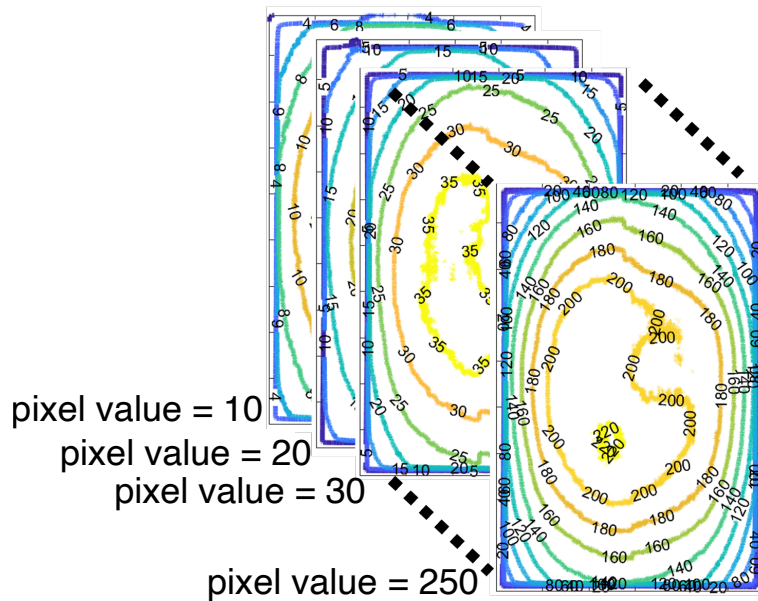
Supplementary Figure. 3 – **Relation between projected light in the DLP plane and measured light in the sample plane.** A series of images in the sample plane were created by projected DLP light of constant intensity, varying in intensity ranging from 10 - 250 in steps of 10. Shown in the figure are the measured contour values of the projected intensity. Both projected and recorded intensities were 8-bit. The corresponding non-uniform sample-plane images were used to generate a lookup table relating projected pixel value to the measured intensity for each position in the sample plane.
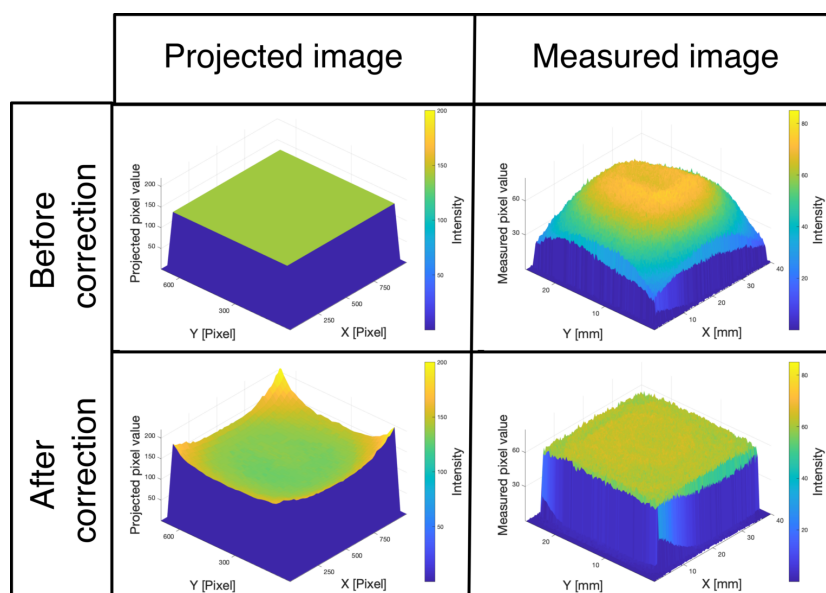
Supplementary Figure. 4 – **Correcting for vignetting in the DLP.** The first row displays an image of uniform intensity, $I = 150$, in the plane of the DLP and the corresponding measured image recorded with a sensor in the sample plane. The area illuminated in the sample plane is 25mm x 40mm. Severe vignetting occurs. The second row shows an image of the intensity in the plane of the DLP after it has been processed to correct for vignetting, resulting in a more uniform image in the sample plane.
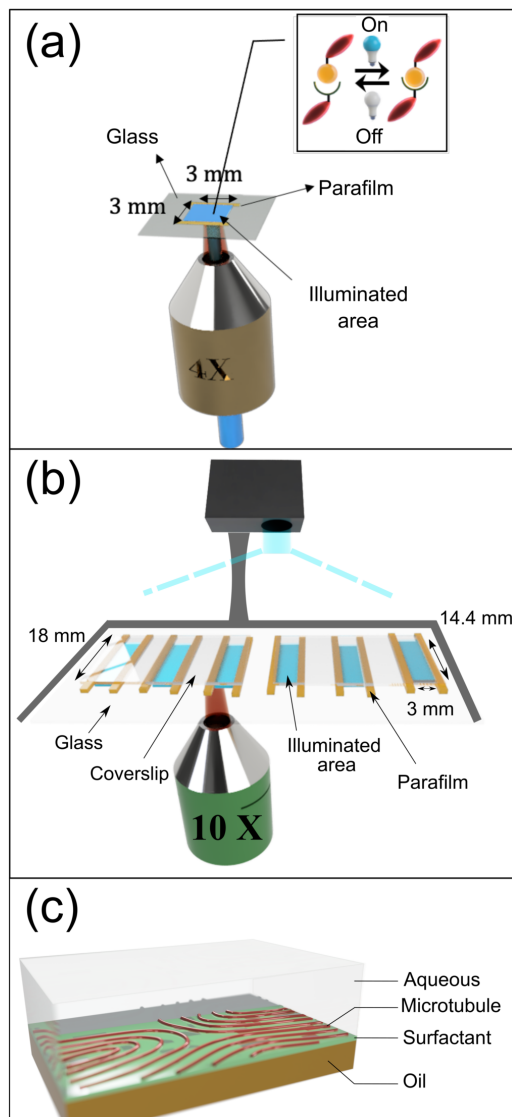
Supplementary Figure. 5 – **Schematic of the experiment.** (a) A single chamber of 3mm x 3mm was used for measurements of the flow speed of the active nematic. The same epi-illumination pathway was used by the computer-controlled DLP projector to activate the nematic and for fluorescence imaging. (b) Up to six independent channels containing active nematics were employed to measure defect density. The widths of each channel varied from 3mm to 6mm, and the lengths were about 18 mm. The projector was mounted to the sample stage so the projected pattern (35 mm x 23 mm) translated with the sample as the sample was moved during imaging. (c) Water-oil interface for 2D nematics showing microtubule network (red), oil phase (yellow), surfactant (green), and aqueous phase (light gray).
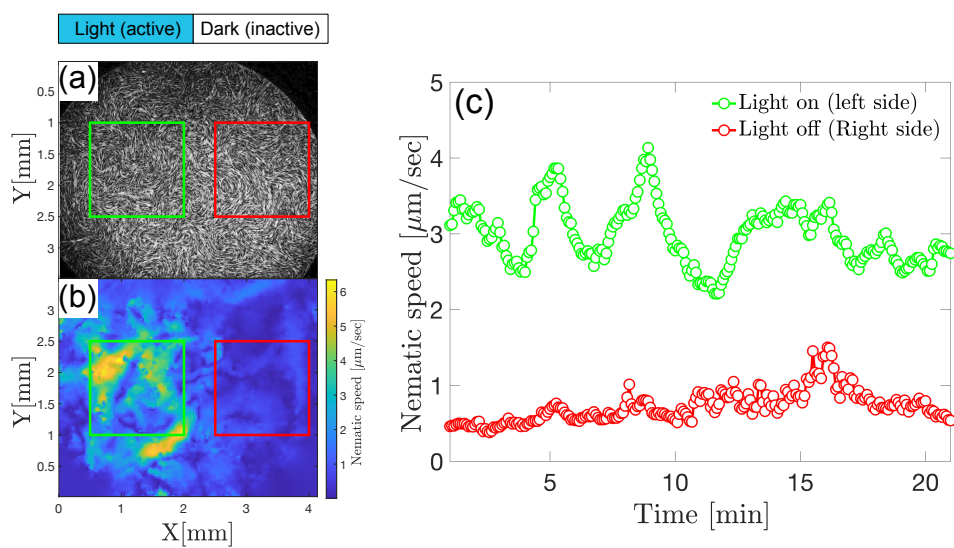
Supplementary Figure. 6 – **Speed of opto-K401 active nematic.** (a) Fluorescence micrograph of an opto-K401 active nematic. The left half was illuminated with sufficient intensity to saturate the velocity and the right half was dark. (b) Spatial map of active nematic speed at an instant of time as determined by PIV analysis. The speed is spatially inhomogeneous. (c) Speed averaged over the regions within the color-coded boxes as a function of time. The speed fluctuates in time. The dark state of opto-K401 had a non-zero velocity and the average ratio of the velocity in the light (active) to dark (inactive) state was about 6.
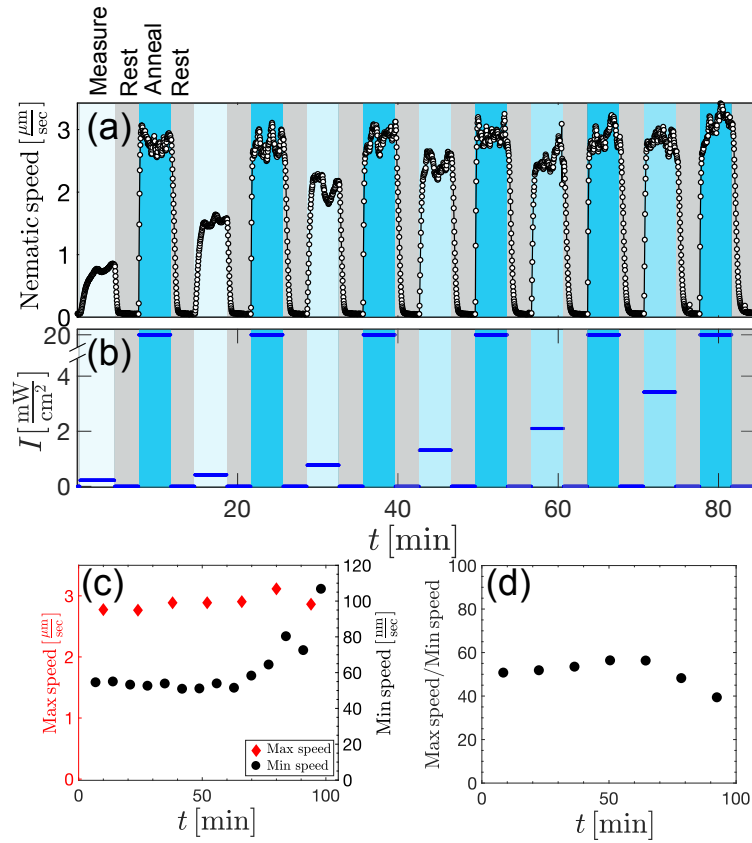
Supplementary Figure. 7 – Applied light determines active nematic flow via light-sensitive motor cluster crosslinking. (a) The average nematic speed (white circles) is plotted against time for time-varying, spatially-uniform light intensities. When the applied light intensity is changed, the nematic responds, reaching steady-state speeds corresponding with the applied light intensity. The average nematic speed was computed from the spatial average of the PIV flow field in the center of the sample cell shown in 5a. (b) A DLP projector is used to apply spatially-uniform light onto an active nematic material composed of microtubules and light-sensitive motor clusters. The plot describes how the intensity of light (blue solid line), I, changes over time in accordance with the light-application protocol composed of 4 repeated steps: anneal at 20 mW/cm^2 for 4 minutes, rest at 0 mW/cm^2 for 3 minutes, measure at varied intensities for 4 minutes, and rest at 0 mW/cm^2 for 3 minutes. (c) The maximum nematic speed (red diamonds, left y-axis) observed at saturating light intensity (20 mW/cm^2) and the minimum speed (black circles, right y-axis) observed at 0 mW/cm^2 are plotted as a function of time. (d) The ratio of the maximum to minimum speeds as a function of time.
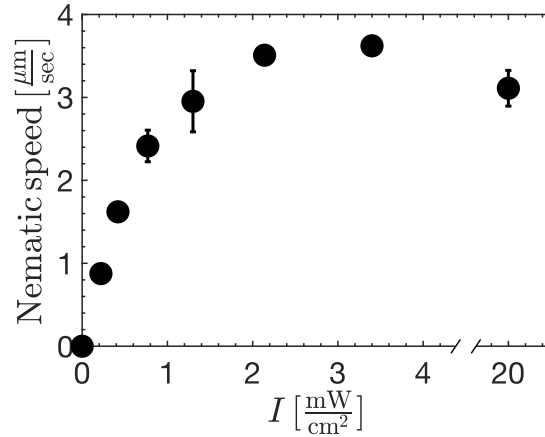
Supplementary Figure. 8 – Speed of opto-K365 active nematic vs. light intensity. Continuous illumination was employed and the speed at steady state was measured using PIV. The data was obtained in the center of the sample cell shown in Supplementary Figure 5(a).
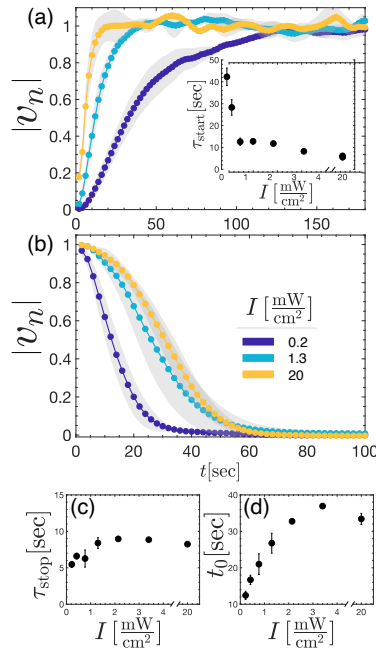
Supplementary Figure. 9 – Nematic flow exhibits transient flow after applied light intensity is changed. (a) The applied light intensity is increased from 0 mW/cm^2 to I. $|v_n(t)|$ (the average speed instantaneous speed, $|v(t)|$, normalized by the steady-state speed, $|v_s(t)|$) increases as a function of elapsed time, t. The grey band represents the standard deviation. *Inset*: The characteristic time constant, τ_{start}, extracted from the function, $|v_n(t)| = 1 - \exp(-t/\tau_{\text{start}})$, is plotted against light intensity, I. (b) The applied light intensity is decreased from I to 0 mW/cm^2. The normalized speed, $|v_n|$, is plotted against elapsed time, t. (c) The data in (b) is fit to $(1 + \exp((t - t_0)/\tau_{\text{stop}}))^{-1}$. Here, τ_{stop} is plotted against light intensity. (d) The time lag, t_0, is plotted against the applied light intensity

Table S 1 – Speed and defect density as a function of intensity

Intensity (mW/cm^2)	Speed (μm/sec)	Defect Density (#/μm^2)
2.1 (High)	2.76 ± 0.38	$(2.67 \pm 0.1) \times 10^{-05}$
0.13 (Low)	1.19 ± 0.36	$(1.72 \pm 0.18) \times 10^{-05}$
	$\sqrt{\text{ratio}}$ (High/Low) 1.51	ratio (High/Low) 1.54
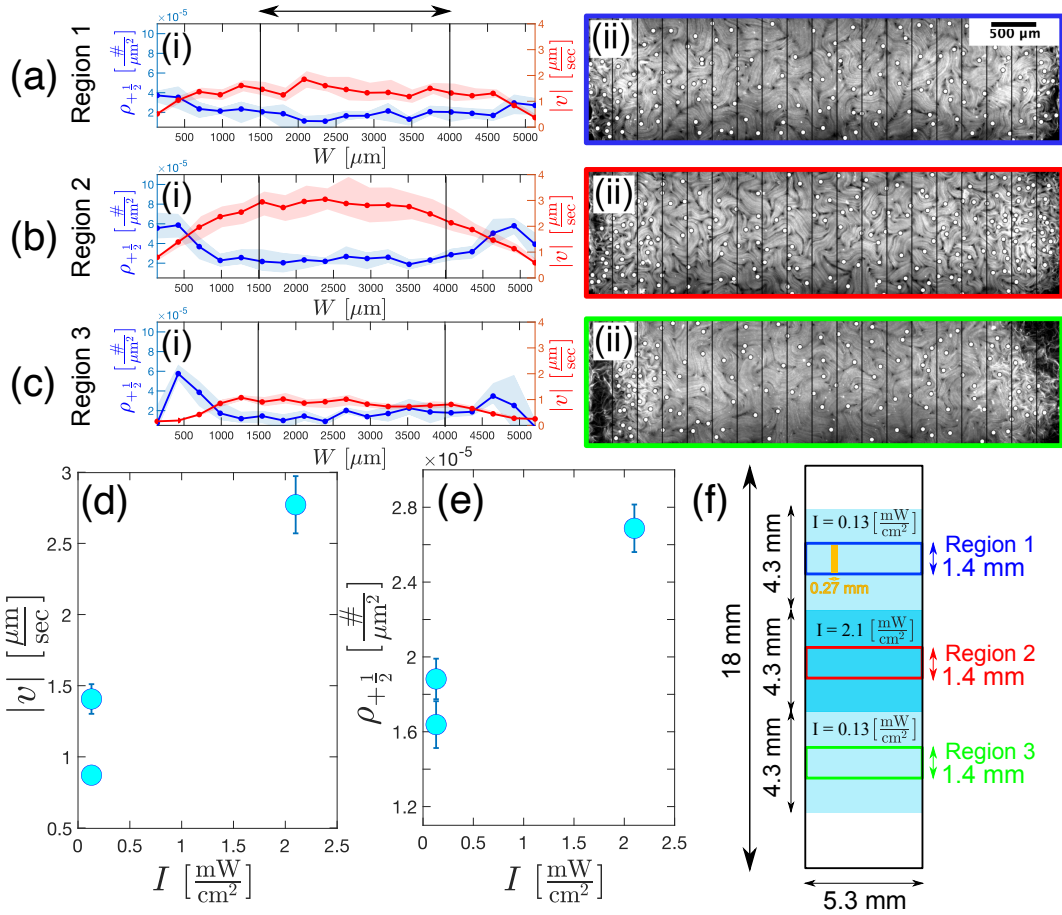
Supplementary Figure. 10 – Nematic speed (v) and defect density ($\rho_{+\frac{1}{2}}$) across the channel width (W).

(a-c) panel (i) The $+\frac{1}{2}$ defect density in blue ($\rho_{+\frac{1}{2}}$) and nematic speed (v) in red across the channel width (W) exposed to blue light in three different regions. The intensity (I) was $I = 0.13$ mW/cm^2 in Region 1 and Region 3, and $I = 2.1$ mW/cm^2 in Region 2. The defect density is high on the channel edge and low at the channel center, while the nematic speed is low near the walls at the channel edge and high away from the walls at the channel center. Each data point in the plots in panel (i) corresponds to averages of $\rho_{+\frac{1}{2}}$ or v in one of the black rectangles (1.4 mm length by 0.27 mm width) in panel (ii). **(a-c) panel (ii)** The corresponding experimental snapshots of the light-activated active nematic in 3 regions, each photograph is 5.3 mm width and 1.4 mm length, a montage of 6 images, and each small black rectangle is 0.27 mm in width and 1.4 mm in length. The white circles show the $+\frac{1}{2}$ defects. Scale bar, 500 μm. The measurements are taken every 4 seconds, and the defects are identified manually. (d) The average nematic speed is calculated using PIV beginning at a distance 1.5 mm from the walls to avoid wall effects. The data included in the average speed is indicated in (a-c) panel (i) as those points between the two vertical black lines in the center of the channel and is from an area of 2.3 mm width by 1.4 length. (e) The average $+\frac{1}{2}$ defect density for each intensity is measured 1.5 mm from the walls. The defects are identified using the MATLAB script mentioned previously. The data included in the defect density is indicated in (a-c) panel (i) as those points between the two vertical black lines in the center of the channel and is from an area of 2.3 mm width by 1.4 length. (f) The entire chamber is 5.3 mm in width by 18 mm in length. The full illuminated area is 5.3 mm in width and 12.8 mm in length, which is divided into 3 areas of different intensities indicated in shades of cyan. Each illuminated area represented in a single cyan rectangle is 5.3 mm in width and 4.3 mm in length. The colored regions indicated as regions 1, 2 and 3 are 5.3 mm in width and 1.4 mm in length. The small orange rectangle of 0.27 mm in width and 1.4 mm in length represents the area over which the data in panel (i) is plotted.
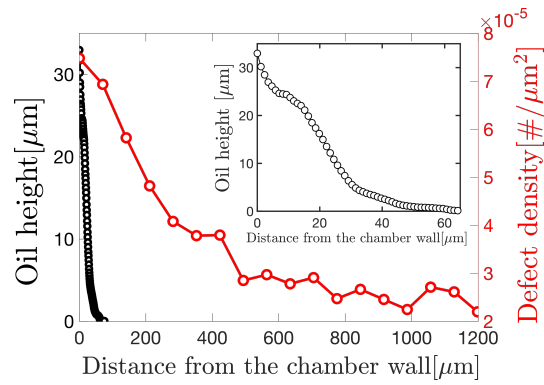
Supplementary Figure. 11 – **Relationship between the defect density and oil height with distance to the wall.** The main plot illustrates the defect density and oil height as functions of the distance to the wall, while the inset focuses on the oil height as a function of the distance to the wall. The oil height has been corrected for the oil index of refraction.
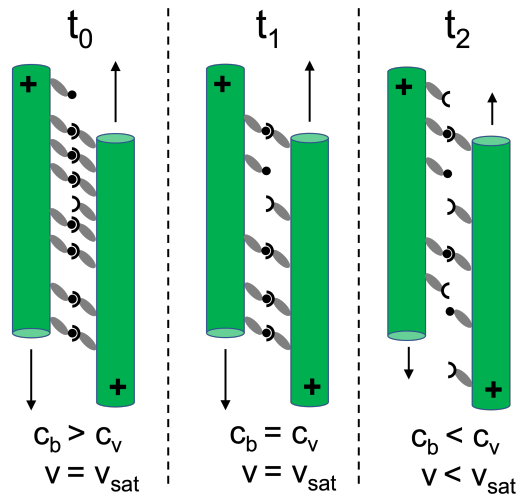
Supplementary Figure. 12 – Model explaining how microtubule speed and bound motor clusters change after strong illumination is extinguished. Initially, at t_0, there is a high concentration of bound motors c_b and the microtubules slide at their maximum speed. After some time, t_1, the concentration of bound motors has decreased to c_v (the concentration of bound motors at which the speed saturates), and the microtubule speed remains constant. At later times, t_2, the concentration of bound motors decreases below c_v and the microtubule speed decreases.

8 Supplementary Videos

8.1 Supplementary Video 1

2D light activated active nematic from opto-K401 under illumination. The fluorescent images are taken with 4X 0.13 NA (Nikon Instruments, CFI Plan Fluor 4X). The exposure time was 100 msec. The scale bar is 500 μ m. The time shows min: sec, and the frame rate is 30 fps.
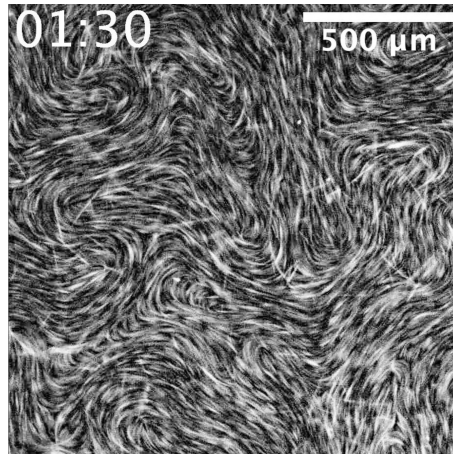
8.2 Supplementary Video 2

2D light activated active nematic from opto-K401 in the dark. The fluorescent images are taken with 4X 0.13 NA (Nikon Instruments, CFI Plan Fluor 4X). The exposure time was 100 msec. The scale bar is 500 μ m. The time shows min: sec, and the frame rate is 30 fps.
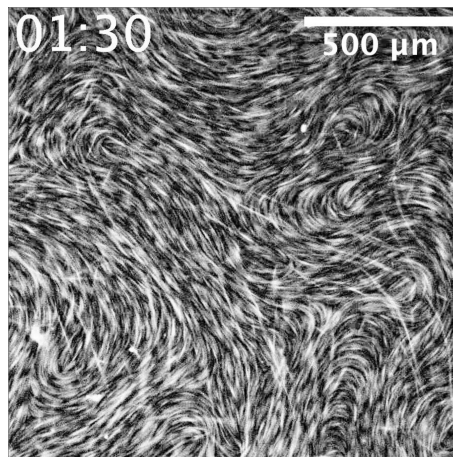
8.3 Supplementary Video 3

Two panels. The right panel is a fluorescent image of a 2D light activated active nematic made with opto-K365 in the 3 mm by 3 mm sample geometry of Supplementary Figure 5(a). The fluorescent images are taken with 4X 0.13 NA (Nikon Instruments, CFI Plan Fluor 4X). The exposure time was 200 msec. The scale bar is 500 μm. The counter represents time in Minutes: Seconds, and the frame rate is 30 fps. The left panel shows the intensity over time. The color red represents intensity in the past and blue the intensity in the future. The red dashed line indicates the current time in the video on the right. This video shows how active nematic changes during the two-step preparation protocol shown in Fig 3.
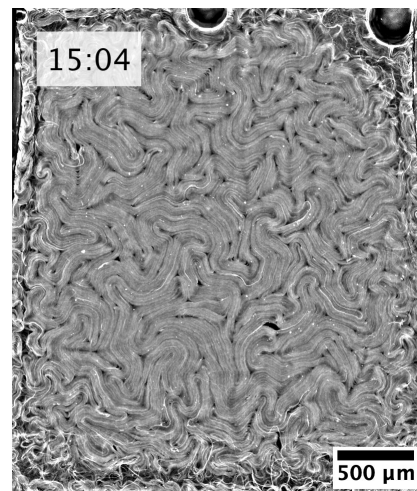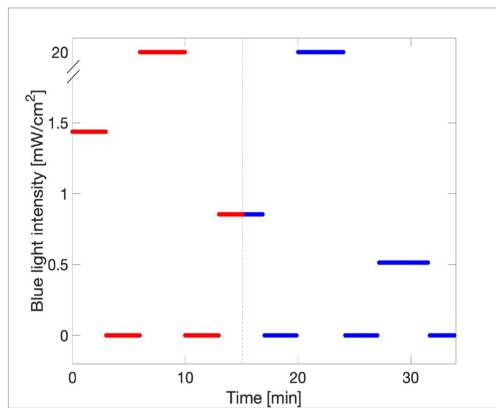
References

[1] W. Thielicke, *Diss. University of Groningen*, 2014.

[2] W. Thielicke and E. Stamhuis, *Journal of open research software*, 2014, **2**, year.

[3] M. M. Norton, *qcon-nematicdefectfinder*, 2023, `https://github.com/wearefor/qcon_nematicdefectfinder`.